MAGNETOHYDRODYNAMICS Vol. 59 (2023), No. 3-4, pp. 281–301
DOI: 10.22364/mhd.59.3-4.3

SST k-ω SIMULATION OF MIXED CONVECTION OF MAGNETOHYDRODYNAMIC FLOW IN A VERTICAL DUCT WITH CONDUCTING WALLS

*Zifeng Hou, Bobo Wu, Yang Cheng, Mingliang Jin, Jie Mao**

School of Mechanical Engineering, Hangzhou Dianzi University, Hangzhou, 310018, China
** e-Mail: maojie@hdu.edu.cn*

Liquid metal magnetohydrodynamic (MHD) flow has a wide range of applications in controlled nuclear fusion, metallurgy, semiconductor, and so on. The liquid metal in ducts or pipes subjected to a strong magnetic field generates Lorentz forces and causes MHD effects. The strong non-uniform thermal gradient generated by nuclear neutron heat in liquid metal blankets causes buoyancy effects. MHD mixed convection flow is a multi-physics and multi-scale coupling problem involving fluid, solid, temperature, and electromagnetic fields, considering the Lorentz force and buoyancy. In this study, mixed convection of magnetohydrodynamic flow in a vertical duct with conducting walls subjected to a non-uniform magnetic field and heat source has been numerically studied using a shear stress transport (SST) Reynolds-averaged Navier-Stokes (RANS) method developed in OpenFOAM. Effects of the Hartmann number (Ha), Reynolds number (Re), and Grashof number (Gr) on MHD mixed convection have been investigated. The results show that an increase in Ha suppresses the generation of reverse flow zones in the duct, stabilizes the flow, and improves the convective heat transfer efficiency at the hot wall. The Nusselt number (Nu) increases with the increase of the Reynolds number when it number increases to a certain extent. The influence of Gr on the velocity field is relatively small in the simulation range. Buoyancy can suppress convective heat transfer at the hot wall. Finally, there is a specific functional relationship between Nu and $\mathrm{Gr}/\mathrm{Ha}^2\mathrm{Re}^2$. These findings provide valuable insights into the behavior of liquid metal flow under MHD mixed convection and have important implications for the design and optimization of liquid metal blankets in thermonuclear fusion reactors.

Key words: SST k-ω, RANS, magnetohydrodynamic, mixed convection, vertical duct, buoyancy.

Introduction.

The magnetohydrodynamic (MHD) flow has a wide range of applications in the study of plasma, MHD generators, magnetic confinement fusion, and other related fields. The liquid metal blanket is crucial for energy transfer in controlled thermonuclear fusion reactors. According to the relative magnitude of the Lorentz force, buoyancy force, inertial force, and viscous force, the flow can be divided into MHD forced convection, natural convection, and mixed convection. Mixed convection is the most complicated and inevitable heat transfer problem in the liquid metal blanket [1]. Though traditionally, experiments have been deployed to study MHD flow, their execution under actual working conditions is challenging [2]. Consequently, numerical simulation has surfaced as a widely employed methodology to investigate thermal nuclear fusion reactors.

Vertical ducts have a well-defined placement in the ITER experimental reactor [3]. The disparity between gravity and buoyancy concerning the fluid direction has a considerable impact on the fluid motion [4]. The mixed convection heat transfer in a vertical duct and in a channel under a transverse strong magnetic field has been studied numerically using a quasi 2D model [5] and linear stability analysis[6]. It is found that the inflection point of the velocity profile moves towards the wall surface as the Hartmann number (Ha) increases. The strong magnetic field effectively suppresses oscillations in the flow and stabilizes the basic flow. Guo and Prasser [7] studied the effect of buoyancy

on the flow of liquid metal fluids in a vertical duct. It is found that buoyancy significantly changes the stress balance near the wall and promotes the upward flow of the fluid at the hot wall.

The above-mentioned papers primarily employ direct numerical simulation (DNS) methods for simulation. Researchers try to use the RANS model to study the MHD duct flow because it can save substantial computing resources. Kenjereš [8] reviewed the numerical method and results about MHD turbulence and heat transfer. Ji and Gardner [9] proposed a modified k-ε model to analyze the flow in a horizontal insulated tube. As the computed data exhibits good agreement with experimental results in the presence of a uniform transverse magnetic field and a constant heat source, the k-ε turbulence model proves to be suitable for the analysis of intricate MHD flows. Kenjereš and Hanjalić [10] modified the source term of the Jis model [9]. The modified model was validated by simulating the experimental test of the electrically insulated rectangular duct flow with the parameters of $\mathrm{Re} = 2\mathrm{e}5$ and $\mathrm{Ha} = 700$. Meng [11] has revised the Kenjereš model [10] and conducted a numerical analysis by comparing the results with the experimental data for a flow with a high Ha, in order to validate the accuracy of the new model. The findings indicate that the model is capable of precise prediction of key flow characteristics, such as the location of the jet and the variations in the Q2D turbulent intensity. By comparing the DNS results, Chen *et al.* [12, 13] discovered that the Kenjereš and Hanjalics model could reasonably predict the electromagnetic effect on the MHD turbulent channel flow. They proposed a nonlinear eddy-viscous k-ω turbulence model integrated with the Kenjereš and Hanjalics model. Zhang [14] presented a revised k-ω model and confirmed its validity through simulation of turbulent MHD flow. The revised k-ω model exhibits a higher accuracy than the standard k-ω model. Moreover, it only used 0.4% computing resources of the DNS.

Previous numerical simulations utilizing the RANS model have primarily focused on forced convection and low Hartmann numbers. In this study, a new SST k-ω turbulence model has been developed and verified, specifically designed for simulating MHD mixed convection. Additionally, we investigated the velocity and temperature distributions under different Ha, Re, and Gr in a vertical duct.

1. Governing equations and numerical models.

1.1. Governing equations. The governing equations of the MHD flow in the liquid metal blanket are

$$\nabla \cdot \mathbf{u} = 0, \tag{1}$$

$$\frac{\partial \mathbf{u}}{\partial t} + (\mathbf{u} \cdot \nabla)\,\mathbf{u} = -\frac{1}{\rho}\nabla p + \nu \nabla^2 \mathbf{u} + \mathbf{f}_{\mathrm{L}} + \mathbf{f}_{\mathrm{B}}, \tag{2}$$

$$\rho C_p \left(\frac{\partial T}{\partial t} + (\mathbf{u} \cdot \nabla)\, T \right) = \nabla \cdot (\lambda \nabla T)\,, \tag{3}$$

$$\mathbf{J} = \sigma\,(-\nabla \phi + \mathbf{u} \times \mathbf{B})\,, \tag{4}$$

$$\nabla \cdot \mathbf{J} = 0, \tag{5}$$

$$\nabla^2 \phi = \nabla \cdot (\mathbf{u} \times \mathbf{B})\,, \tag{6}$$

The induced electric potential equation in the solid wall is

$$\nabla^2 \phi_{\mathrm{s}} = 0. \tag{7}$$

In the above formulas, t represents the time, $\mathbf{B}$ represents the strength of the magnetic field; $\mathbf{u}$, p, $\mathbf{J}$, T, ϕ, ϕ_s stand for the velocity, pressure, electric current density, temperature, induced potential of the fluid, and induced potential in the solid wall; ρ, ν, C_p, λ, σ are the relevant physical parameters, which represent density, kinematic viscosity, isobaric specific heat capacity, thermal conductivity of the liquid metal and the electric conductivity of the fluid, respectively. The $\mathbf{f}_L = \mathbf{J} \times \mathbf{B}/\rho$ in Eq. (2) is the Lorentz force, $\mathbf{f}_B = -\beta\mathbf{g}(T - T_0)$ is the buoyancy term based on Boussinesq assumption, with β being the volume expansion coefficients, $\mathbf{g}$ is the acceleration of gravity, T_0 represents the initial temperature of the metal fluid entering the duct. The impact of viscous dissipation and Joule dissipation is negligible in the range of the parameter in this paper according to [15–17]. The benchmark case used for validation of the model in section 3 also neglects these dissipation effects in the energy equation. In all numerical simulation cases, the influence of thermal neutron radiation is not considered.

The important non-dimensional parameters involved in this paper are the following: the Hartmann number $\mathrm{Ha} = BL\sqrt{\sigma/\rho\nu}$; the square of this equation represents the ratio between the Lorentz force and the viscous force. The Reynolds number $\mathrm{Re} = U_0 L/\nu$ represents the ratio of inertial to viscous force. The Grashof number $\mathrm{Gr} = g\beta\Delta T L^3/\nu^2 = g\beta q L^4/(\lambda\nu^2)$ represents the ratio of buoyancy to viscous force, q is the heat flux per unit area on the heating wall. The wall conductance ratio $c = \sigma_w t_w/\sigma L$ represents the ratio of solid conductivity to fluid conductivity, where σ_w is the conductivity of the solid wall, and t_w is the wall thickness of the duct. The equation for the average Nusselt number on the hot wall surface reads

$$\mathrm{Nu} = \frac{1}{S_h}\iint\limits_h \frac{hL}{\lambda}\mathrm{d}x\mathrm{d}y = \frac{1}{S_h}\iint\limits_h \frac{qL}{\lambda(T - T_0)}\mathrm{d}x\mathrm{d}y, \tag{8}$$

where h represents the heating surface, S_h is the area of the heating surface, and T_0 is the inlet temperature. It represents the dimensionless temperature gradient normal to the wall used to measure the intensity of convective heat transfer. All the dimensionless parameters mentioned above are calculated using the characteristic length L, which is half of the duct's width.

1.2. MHD turbulence model based on the RANS method. In this study, according to the relationship between k, ε, and ω (specific dissipation rate), the Kenjereš and Hanjalić MHD basic source term has been referenced [10], and the basic structure of the MHD SST k-ω model is derived as

$$\frac{\partial k}{\partial t} + \frac{\partial (U_i k)}{\partial t} = \tilde{P}_k - \beta^* k\omega + \frac{\partial}{\partial x_i}\left[(\nu + \sigma_k \nu_t)\frac{\partial k}{\partial x_i}\right] + S_k^M, \tag{9}$$

$$\frac{\partial \omega}{\partial t} + \frac{\partial (U_i \omega)}{\partial t} = \alpha S^2 - \beta\omega^2 + \frac{\partial}{\partial x_i}\left[(\nu + \sigma_{\omega 1}\nu_t)\frac{\partial \omega}{\partial x_i}\right] + 2(1 - F_1)\sigma_{\omega 2}\frac{1}{\omega}\frac{\partial k}{\partial x_i}\frac{\partial \omega}{\partial x_i} + S_\omega^M. \tag{10}$$

The relevant expression for turbulent viscosity is

$$\nu_t = \frac{a_1}{\max(a_1\omega, SF_2)}, \tag{11}$$

where S is the estimated size of the strain rate and generally takes the value of 10. The switching functions F_1 and F_2 are defined as

$$F_2 = \tanh\left[\left[\max\left(\frac{2\sqrt{k}}{\beta^*\omega y}, \frac{500\nu}{y^2\omega}\right)\right]^2\right], \tag{12}$$

$$F_1 = \tanh\left\{\left\{\min\left[\max\left(\frac{\sqrt{k}}{\beta^*\omega y}, \frac{500\nu}{y^2\omega y}\right), \frac{4\sigma_{\omega 2}k}{CD_{k\omega}y^2}\right]\right\}^4\right\}. \tag{13}$$

In Eqs. (12) and (13), y is the distance from the inner mesh node to the nearest wall.

$$CD_{k\omega} = \max\left(2\rho\sigma_{\omega 2}\frac{1}{\omega}\frac{\partial k}{\partial x_i}\frac{\partial \omega}{\partial x_i}, 10^{-10}\right), \tag{14}$$

$$P_k = \nu_{\mathrm{t}}\frac{\partial U_i}{\partial x_j}\left(\frac{\partial U_i}{\partial x_j} + \frac{\partial U_j}{\partial x_i}\right) \rightarrow \tilde{P} = \min\left(P_k, 10\beta^* k\omega\right). \tag{15}$$

The relevant model coefficients are as follows:
$\alpha_1 = 5/9$, $\alpha_2 = 0.44$, $\beta_1 = 3/40$, $\beta_2 = 0.0828$, $\beta^* = 9/100$,
$\sigma_{k1} = 0.85$, $\sigma_{k2} = 1$, $\sigma_{\omega 1} = 0.5$, $\sigma_{\omega 2} = 0.856$, $a_1 = 0.31$.
The new MHD source terms are:

$$S_k^{\mathrm{M}} = -\frac{\sigma}{\rho}B^2 k C_4 \exp\left(-C_5\frac{\sigma}{\rho}B^2\frac{1}{\omega}\right), \tag{16}$$

$$S_\omega^{\mathrm{M}} = -\frac{\sigma}{\rho}B^2 \omega C_4 \exp\left(-C_5\frac{\sigma}{\rho}B^2\frac{1}{\omega}\right). \tag{17}$$

The model coefficients C_4 and C_5 in Eqs. (16) and (17) are 1.6219 and 0.27, respectively. The modified SST model is defined as SSTMHD.

Fig. 1 illustrates the solving process of the mixed convection heat transfer solver.

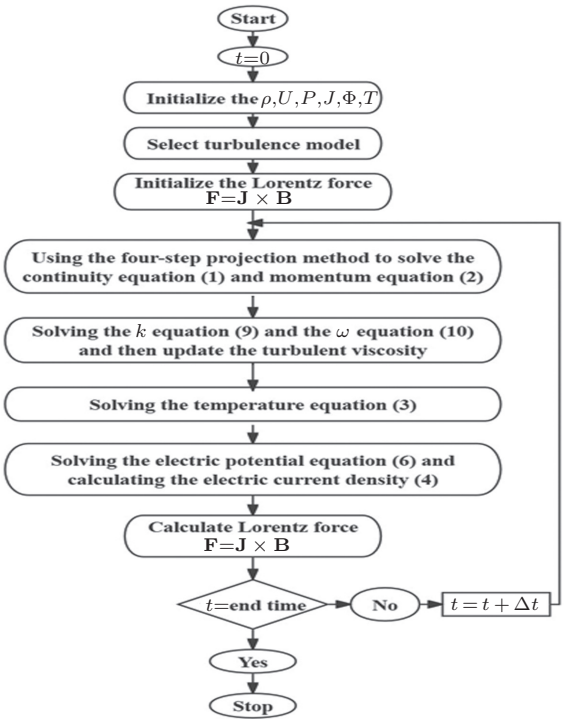

Fig. 1. Flowchart of the mixed convection heat transfer solve.

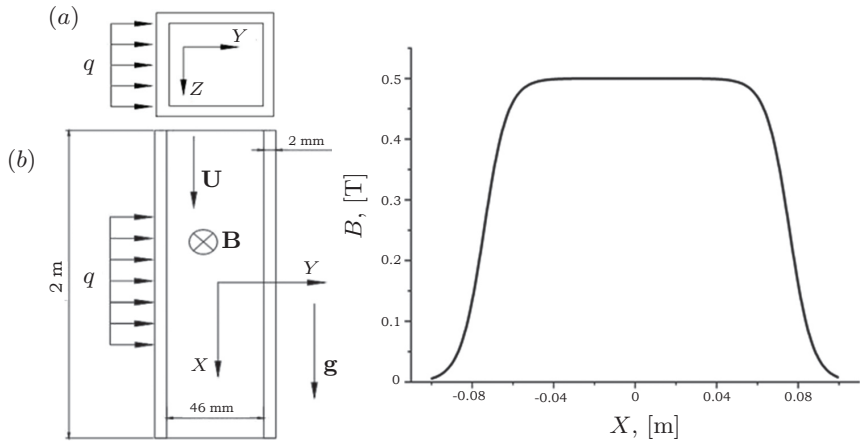

Fig. 2. (*a*) Physical model plan view of the duct, (*b*) elevation view, and (*c*) magnetic field distribution of the duct.

1.3. Geometry and parameters. Smolentsev *et al.* [18] compared the results of a mixed convection flow in a conductive duct using DNS based on OpenFOAM. We choose the physical model as a benchmark case to validate the SSTMHD model, as shown in Fig. 2. The Fig. 2*a* is the plan view of the duct, and Fig. 2*b* is elevation view. The duct is square with the length of 2 m and its cross-section is 5 cm × 5 cm and a wall thickness of $t_w = 2$ mm. The characteristic length is $L = 23$ mm. Under the effect of a non-uniform magnetic field, the liquid metal PbLi flows downward along the x-axis in the duct.

The uniform magnetic field has a constant value $B_0 = 0.5$ T (Fig. 2*c* takes $B_0 = 0.5$ T as an example), whose length is approximately 0.8 m ($-0.4\,\text{m} < x < 0.4\,\text{m}$). Eqs. (18) and (19) are used to generate the ascending and descending segments of the non-uniform magnetic field in the numerical simulation for $\gamma = 0.2$, $a = 0.8$, $b = 0.5$, $c = -0.7$, $d = 0.5$.

The ascending and descending segments of the magnetic field are

$$B = \frac{1 + \tanh\left[\gamma(x + a)/L - b\right]}{2} B_0 \tag{18}$$

$$B = \frac{1 + \tanh\left[\gamma(x + c)/L - d\right]}{2} B_0. \tag{19}$$

The physical parameters of PbLi are the following: the density $\rho = 9486\,\text{kg}\cdot\text{m}^{-3}$, the kinematic viscosity $\nu = 2.27\times10^{-7}\text{m}^2\text{s}^{-1}$, the thermal conductivity $\lambda = 13.1\,\text{W}/(\text{m}\cdot\text{k})$, and the electric conductivity $\sigma = 7.89\times10^5\,(\Omega\cdot\text{m})^{-1}$. The solid wall material is stainless steel (SS394) with the conductivity $\sigma = 1.09\times10^6\,(\Omega\cdot\text{m})^{-1}$ and thermal conductivity $\lambda = 19\,\text{W}/(\text{m}\cdot\text{k})$.

Table 1 lists the parameters used in the numerical simulation calculations, in which Case 1 is the benchmark case. When utilizing the turbulence model for fluid heat transfer calculations, it is essential to consider the turbulent Prandtl number (Pr_t). The calculation formula of Pr_t proposed by Jischa and Rieke [19] was used:

$$\text{Pr}_t = 0.9 + \frac{182.4}{\text{Pr}\,\text{Re}^{0.888}}\ . \tag{20}$$

The Prandtl number of liquid PbLi at 300°C is $\text{Pr} = 0.032$. During the calculation, it was found that an increase in Gr would significantly increase the amount of computation

Table 1. Calculation parameters.

	Ha	Re	Gr	Pr_t	B_0[T]	U[m/s]	q[KW/m^2]	Nu
Case 1	220	3040	$2.88{\cdot}10^7$	5.5	0.5	0.03	40	2.98
Case 2	440	3040	$2.88{\cdot}10^7$	5.5	1	0.03	40	3.5
Case 3	660	3040	$2.88{\cdot}10^7$	5.5	1.5	0.03	40	4.42
Case 4	1100	3040	$2.88{\cdot}10^7$	5.5	2.5	0.03	40	4.78
Case 5	660	6080	$2.88{\cdot}10^7$	3.2	1.5	0.06	40	5.46
Case 6	660	9120	$2.88{\cdot}10^7$	2.6	1.5	0.09	40	7.09
Case 7	660	15200	$2.88{\cdot}10^7$	2	1.5	0.15	40	8.8
Case 8	660	9120	$1.44{\cdot}10^8$	2.6	1.5	0.09	200	7.35
Case 9	660	9120	$2.88{\cdot}10^8$	2.6	1.5	0.09	400	7.15

required. The total computational time is 13824 and 30720 core hours for Case 1 and Case 9, respectively. Compared to Case 1, the computing cost of Case 9 increased by about 220%. Due to the constrained computational resources, we were unable to satisfy scenarios with significantly higher Gr numbers, such as $\mathrm{Gr} = 10^{10} - 10^{12}$.

It is noteworthy to emphasize that the DNS simulations[18] referred to in this study required a total computational time of approximately 85200 core hours. Conversely, when the SSTMHD model was used to simulate the same case, the total computational time required was about 13824 core hours. Thus, compared to DNS, employing the SSTMHD turbulence model can lead to a reduction in computational workload by approximately 83%.

1.4. Boundary conditions and grids arrangement. The velocity boundary is a fixed normal component U_0 applied at the inlet, and zero gradients at the outlet. No-slip boundary condition is used at the inner wall of the duct. The pressure value at the outlet is zero, and a zero gradient is applied at the inlet and the walls.

A fixed temperature of $T_0 = 573.15\,\mathrm{K}$ is given at the inlet, and a fixed temperature gradient $\partial T/\partial z = q/L$ is given at the heating surface. Other surfaces inside the duct are heat insulated and have a zero gradient boundary condition.

A non-uniform grid was used at the cross-section of the duct. The number of nodes was 80×80 to ensure that there are 7 grids in the Ha layer and 25 grids in the parallel layer. Uniform 530 nodes were used along the streamwise direction, and the final grid number was 3392000.

1.5. Numerical methods. The MHD transient solver embedded consistent and conservative methods [20] coupled with fluid and solid walls has been validated [21, 22]. In this paper, the modified turbulent model SSTMHD has been complied in the solver in OpenFOAM.

In this study, the pressure and electric potential equation is solved by a pre-conditioned conjugate gradient (PCG) matrix solver and a geometric-algebraic multi-grid (GAMG) pre-conditioned conjugate gradient solver. The pre-conditioned bi-conjugate gradient (PBiCG) matrix solver combined with a diagonal incomplete-LU (DILU) is used to solve the velocity and temperature equation.

The second-order Crank–Nicolson scheme with a coefficient of 0.5 is used to discrete the time in the simulation, and the Gauss linear scheme is used for the convective, gradient, and diffusion terms. The convergence tolerances are set to $1{\cdot}10^{-8}$ for ϕ, $1{\cdot}10^{-10}$ for T, $1{\cdot}10^{-6}$ for P, $1{\cdot}10^{-7}$ for U, while the time step is set to $1{\cdot}10^{-4}\,\mathrm{s}$.

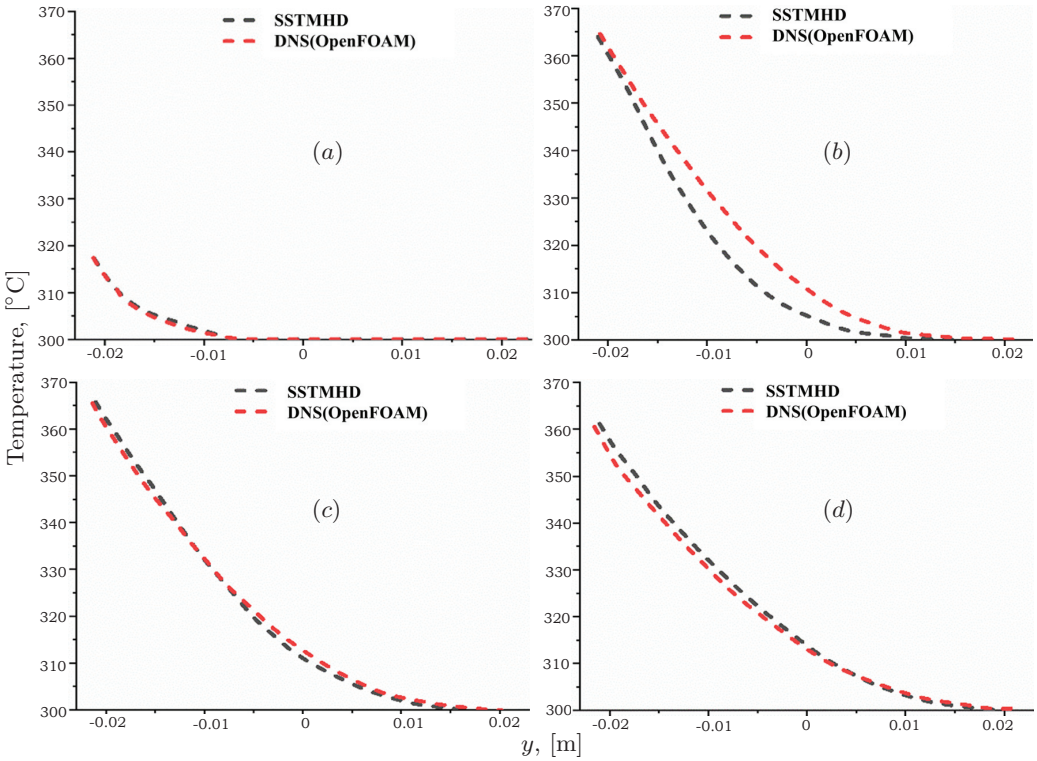

Fig. 3. Time-averaged temperature profiles along the y-axis obtained from the SSTMHD and DNS (OpenFOAM) at $z = 0$, (*a*) $x = -0.15$ m, (*b*) $x = 0.05$ m, (*c*) $x = 0.15$ m, (*d*) $x = 0.25$ m.

2. Validation results of the benchmark case.

The time-averaged temperature profiles were obtained from both the SSTMHD model and the DNS (OpenFOAM) on the central surface $z = 0$ at $x = -0.15$ m, $x = 0.05$ m, $x = 0.15$ m, and $x = 0.25$ m, as shown in Fig. 3. In the first half of the heating region $x = -0.15$ m, as Fig. 3*a*, there is no apparent heating effect, and the heat is transferred downward with the flow. Therefore, the temperature does not rise in the zone between $y = -0.005$ m and $y = 0.023$ m. On the other hand, the temperature rises from $y = -0.023$ m to $y = -0.005$ m as a result of insufficient heating. As shown in Fig. 3*b*, the heating impact is strong in the heating core region $x = 0.05$ m, and the temperature increases to 365°C close to the hot wall.

The temperature profiles generated from the DNS (OpenFOAM) and the SSTMHD model agree well. The center of the duct, between $y = -0.015$ m and $y = 0.015$ m, has the largest temperature differential, with a maximum difference of 7°C, as shown in Fig. 3*b*. The temperature profiles produced from the SSTMHD model and DNS are marginally different in the bottom portion of the heating section, at $x = 0.15$ m and $x = 0.25$ m, as illustrated in Figs. 3*c*,*d*. Overall, the SSTMHD model is precise in temperature simulation.

The velocity profiles from the SSTMHD and DNS (OpenFOAM) at $x = -0.15$ m, $x = 0.05$ m, $x = 0.15$ m, and $x = 0.25$ m are presented in Fig. 4. In the first half of the heated section at $x = -0.15$ m, as shown in Fig. 4*a*, the SSTMHD models velocity is a typical M-shaped distribution, but a reversed flow is observed near the hot wall from the DNS (OpenFOAM). As the liquid metal flows downward, it is heated, with the

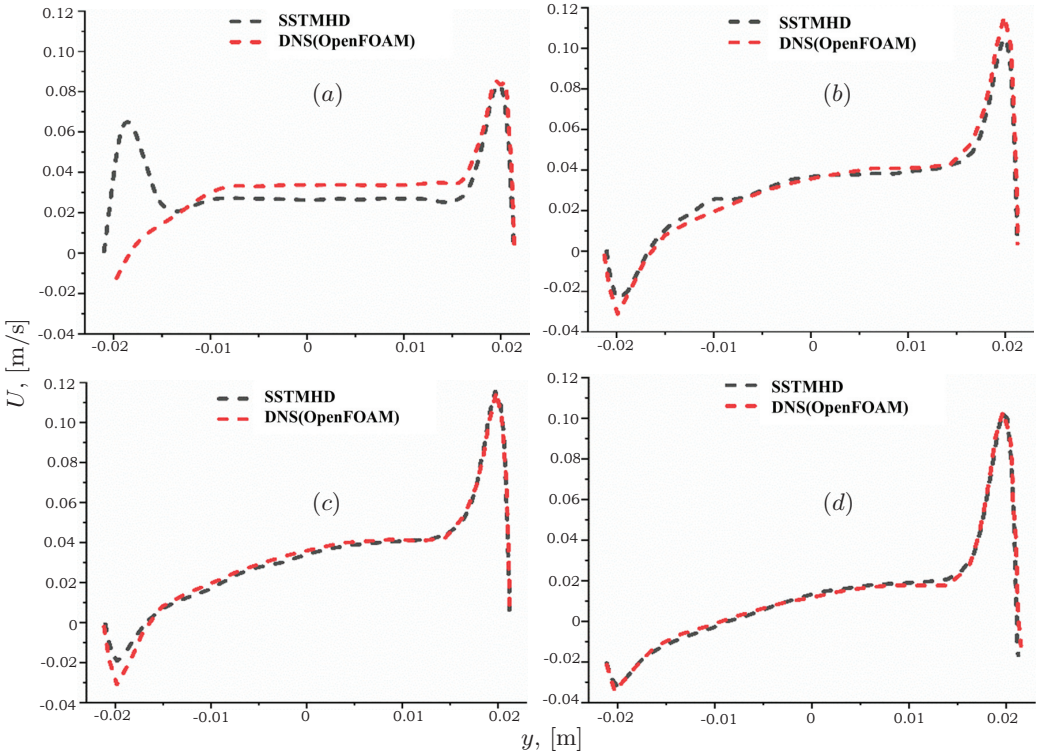

Fig. 4. Time-averaged velocity profiles obtained from the SSTMHD and DNS (OpenFOAM) at $z = 0$, (*a*) $x = -0.15$ m, (*b*) $x = 0.05$ m, (*c*) $x = 0.15$ m, (*d*) $x = 0.25$ m.

temperature increasing continuously. According to Fig. 4*b*, the buoyancy effect becomes more pronounced, and a reversed flow is seen in the SSTMHD model profile. The velocity profiles in the middle of the duct fit quite well, and the velocity peaks close to the walls from the SSTMHD model at $x = 0.05$ m are a bit lower than those from the DNS. The model's velocity fits the results from the DNS (OpenFOAM) well at $x = 0.15$ m except for a slightly less velocity near the hot wall, as seen in Fig. 4*c*. The two sets of results match well at $x = 0.25$ m, as seen in Fig. 4*d*.

The total velocity variation leads to the conclusion that the buoyancy effect caused by the intense non-uniform temperature distribution causes the flow near the hot wall to reverse. Within the zone of reversed flow, the velocity peak value initially rises and subsequently falls, whereas at the cold wall it rises initially and stays the same. This evolving process can be faithfully simulated using the SSTMHD model.

3. Results and discussion.

3.1. Hartmann number effects on mixed convection. Fig. 5 shows the time-averaged velocity distribution at the center section ($z = 0$ m) of the duct at $\mathrm{Gr} = 2.88 \times 10^7$, $\mathrm{Re} = 3040$. The time-averaged values are obtained by taking the time mean within a quasi- stationary period. After reaching a quasi-steady state, the time mean is calculated based on the results from 1×10^4 time-steps. The liquid metal enters the duct with a uniform velocity from the inlet. Prior to entering the magnetic field, viscous boundary layers manifest on both sides of the duct. As the fluid flows downstream, a light blue low-velocity zone appears in the middle of the duct, and the low-velocity zones on both sides gradually disappear. The flow gradually develops into a typical M-shaped velocity

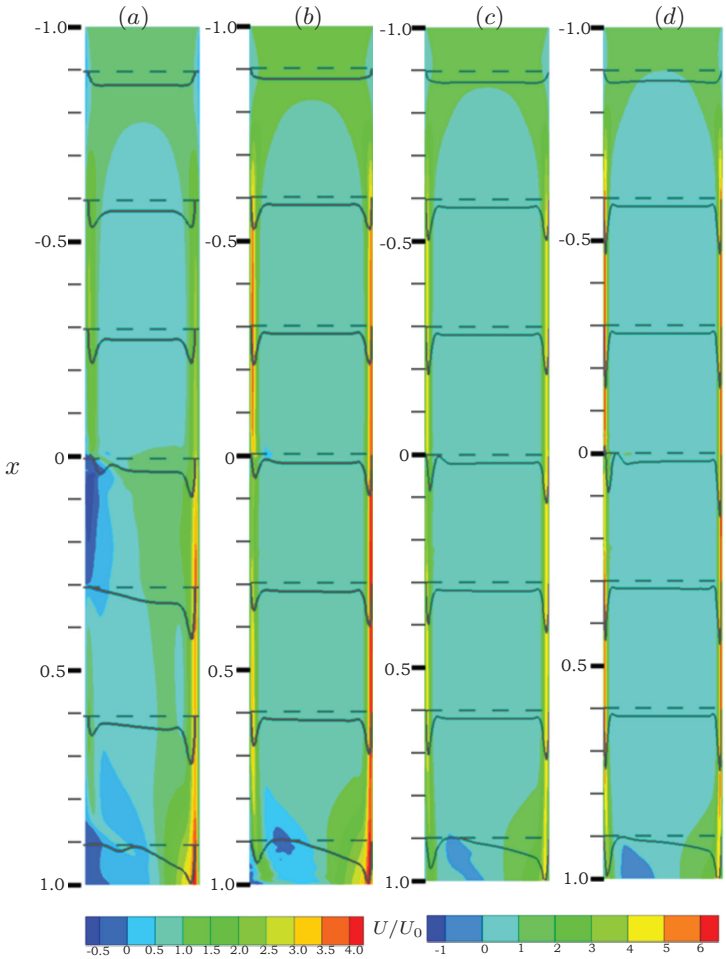

Fig. 5. Colored contours of the time-averaged velocity in the central section at $z = 0\,\mathrm{m}$ for $\mathrm{Gr} = 2.88 \times 10^7$, $\mathrm{Re} = 3040$, (*a*) $a = 220$, (*b*) $\mathrm{Ha} = 440$, (*c*) $\mathrm{Ha} = 660$, (*d*) $\mathrm{Ha} = 1100$. The black dashed line is a reference line taken every 13 characteristic lengths. The black solid lines represent the velocity profile of the reference line (these velocity solid lines are uniformly scaled to ensure readership).

profile after entering the uniform magnetic field ($x \leq -0.3\,\mathrm{m}$). As Ha increases, the position of the light blue low-velocity zone gradually extends upstream. This is due to the fact that the MHD effect intensifies as the fluid enters the magnetic field's rising section. The width of the high-velocity area (boundary layer of velocity) on both sides of the duct becomes narrower, but the peak velocity becomes larger.

The high-velocity jet zone vanishes at the middle position ($x = 0\,\mathrm{m}$) on the left wall, as shown in Fig. 5*a*. Additionally, a dark blue reverse flow zone manifests itself due to the fluid's one-sided heating producing an uneven temperature field and causing upward buoyancy. When the upward buoyancy, Lorentz, and viscous force are greater than the downward inertial force, the reverse flow occurs. The corresponding peak value of the jet near the right cold wall increases as Ha increases. Only a trivial reverse flow spot appears near the wall at $x = 0$ m, indicating that the influence of buoyancy gradually

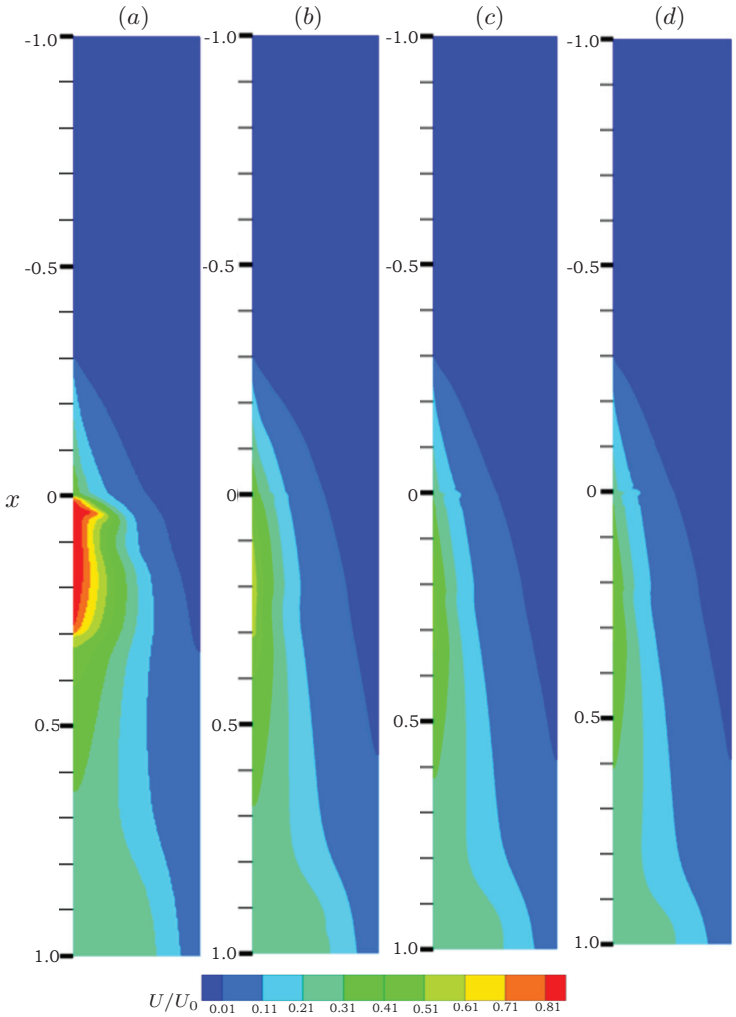

Fig. 6. Colored contours of the time-averaged dimensionless temperature on the plane at $z = 0$ m for $\mathrm{Gr} = 2.88 \cdot 10^7$, $\mathrm{Re} = 3040$. (*a*)$\mathrm{Ha} = 220$, (*b*) $\mathrm{Ha} = 440$, (*c*) $\mathrm{Ha} = 660$, (*d*) $\mathrm{Ha} = 1100$.

decreases, as shown in Figs. 5*c*,*d*.

Near the outlet of the duct (the descending section of the non-uniform magnetic field), a reverse flow appears again near the left wall because the decrease of the magnetic field decreases the Lorentz force significantly, and the upward buoyancy dominates. This finding agrees with the outcomes of Smolentsev's research [20].

The heat transfer mode of the MHD duct flow includes heat conduction and convection. Fig. 6 illustrates the temperature distribution at the center section ($z = 0$). The time-averaged dimensionless temperature θ is defined as:

$$\theta = \frac{T - T_0}{\Delta T} \tag{21}$$

where ΔT represents the characteristic temperature difference defined as . The high-temperature layer on the left wall disappears and the range of temperature transfer from left to right also decreases, as shown in Fig. 6. When $\mathrm{Ha} = 220$, there is a significant

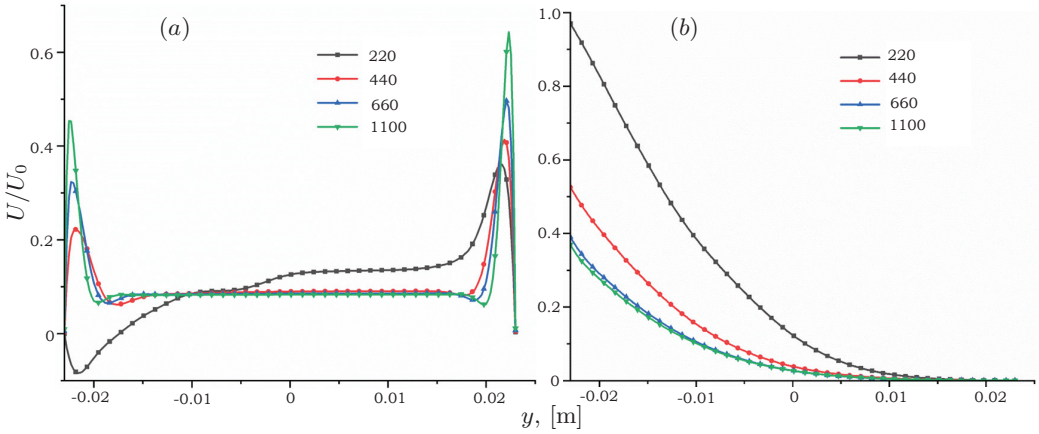

Fig. 7. Profiles of (*a*) time-averaged velocity and (*b*) time-averaged temperature along the y-axis at $x = 0.1$ m and $z = 0$ m for $\mathrm{Gr} = 2.88 \times 10^7$, $\mathrm{Re} = 3040$.

region of the reverse flow at m that corresponds to the primary turbulent zone inside the duct, where heat transfer predominantly occurs through convection. At higher Ha, the flow has become relatively stable. The primary heat transfer method is conduction. This is consistent with Rhodes [23] results.

Fig. 7 presents the time-averaged velocity and temperature along the y-axis. As Ha increases, the reverse flow near the heating wall diminishes. The velocity profile undergoes an asymmetrical distribution due to the influence of buoyancy. At $\mathrm{Ha} = 220$, no thin jet along the streamwise direction is observed near the wall due to the buoyancy effect dominance over the inertial effect at this position. As Ha increases, the high-velocity jet zone on both sides of the duct becomes narrower, and the peak velocity increases. Furthermore, the maximum temperature steadily drops because of the increasing velocity jet near the hot wall.

3.2. Reynolds number effects on mixed convection. Fig. 8 shows colored contours of the time-averaged velocity in the central section. There is no notable change in the middle and upstream of the duct. However, a reverse flow occurred near the heating surface on the left side of the duct ($x = -0.05$ m) at $\mathrm{Re} = 6080$, while there is no reverse flow at other parameters. It shows that there is a critical Reynolds number $\mathrm{Re}_{\mathrm{cr}}$ between $\mathrm{Re} = 3040$ and 9120. The reverse flow gradually appears with the increase of Re as $\mathrm{Re} < \mathrm{Re}_{\mathrm{cr}}$, then it disappears as $\mathrm{Re} > \mathrm{Re}_{\mathrm{cr}}$. The reverse flow near the outlet disappears with the increase of Re, as shown in Fig. 8. This phenomenon is due to the fact that the pressure rises with increasing Re. Therefore, the upward buoyancy could not dominate. As a result, the reverse flow disappears.

Fig. 9 shows the colored contours of the time-averaged dimensionless temperature in the central section of the duct. The heated zone along the y-axis and the temperature stratification both diminish as Re increases. The heat transfer law variation with Re is in agreement with Zhang's [5] results. As Re increases, the forced convection effect enhances, resulting in a predominant heat transfer in the flow direction and in a weakened transverse thermal convection along the y-axis. The maximum value of the dimensionless temperature keeps falling with Re increases.

Fig. 10 presents the time-averaged velocity and temperature along the y-axis. As depicted in Fig. 10*a*, the velocity of the jet near the hot wall decreases to its minimum at $\mathrm{Re} = 6080$ and subsequently increases. This is consistent with the results in Fig. 8. It

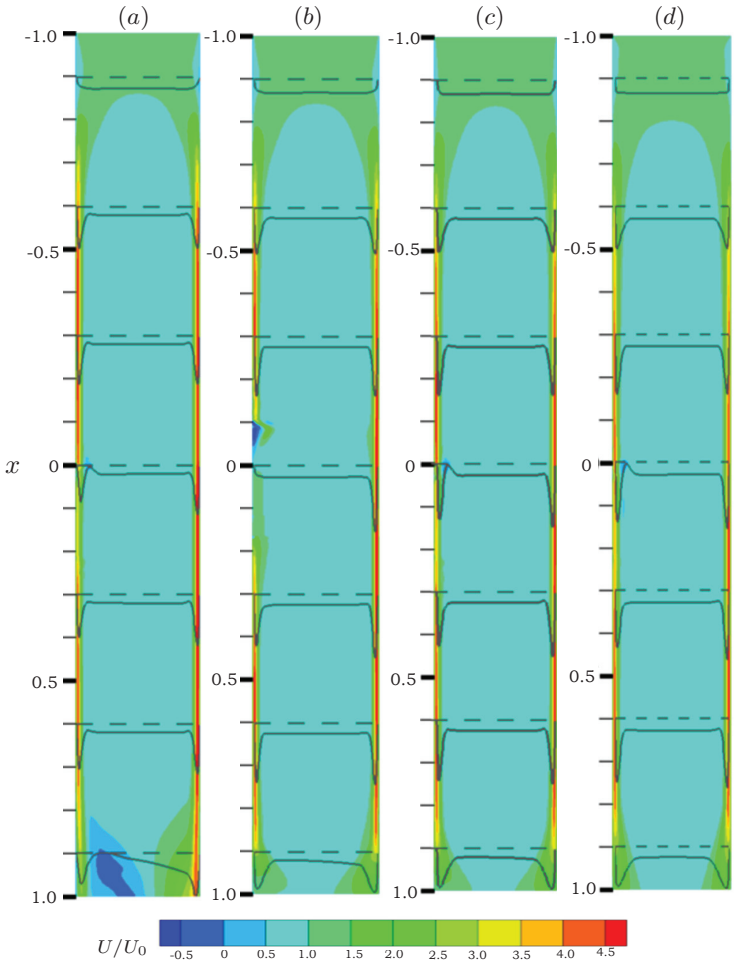

Fig. 8. Colored contours of the time-averaged velocity in the central section at $z = 0$ m for $\mathrm{Gr} = 2.88 \cdot 10^7$, $\mathrm{Ha} = 660$: (*a*) $\mathrm{Re} = 3040$, (*b*) $\mathrm{Re} = 6080$, (*c*) $\mathrm{Re} = 9120$, (*d*) $\mathrm{Re} = 15200$. The black dashed line is a reference line taken every 13 characteristic lengths. The black solid lines represent the velocity profile of the reference line (these velocity solid lines are uniformly scaled to ensure readership).

implies that the peak value of the jet decreases with Re increase as $\mathrm{Re} < \mathrm{Re}_{\mathrm{cr}}$. After that, the peak value of the jet grows in reaction to the increase in Re as $\mathrm{Re} > \mathrm{Re}_{\mathrm{cr}}$. Fig. 10*b* demonstrates that as Re increases, the maximum temperature steadily drops and the heat transmission range along the y-axis gets narrower.

Fig. 11 shows the Lietex vorticity distributed along the duct. Liutex is the third-generation vortex recognition method proposed by Liu *et al.* [24, 25]. The Liutex vector is defined as

$$\mathbf{R} = \left(\langle \mathbf{V}_\omega, \mathbf{r} \rangle - \sqrt{\langle \mathbf{V}_\omega, \mathbf{r} \rangle^2 - 4\lambda_{\mathrm{ci}}^2} \right) \mathbf{r}, \tag{22}$$

where $\mathbf{V}_\omega$ is the vorticity vector, $\mathbf{r}$ is the real eigenvector of $\nabla \mathbf{v}$, and λ_{ci} is the complex conjugate characteristic pair of the velocity gradient. Under the influence of a strong magnetic field, the vortices exhibit typical characteristics of a quasi-two-dimensional tur-

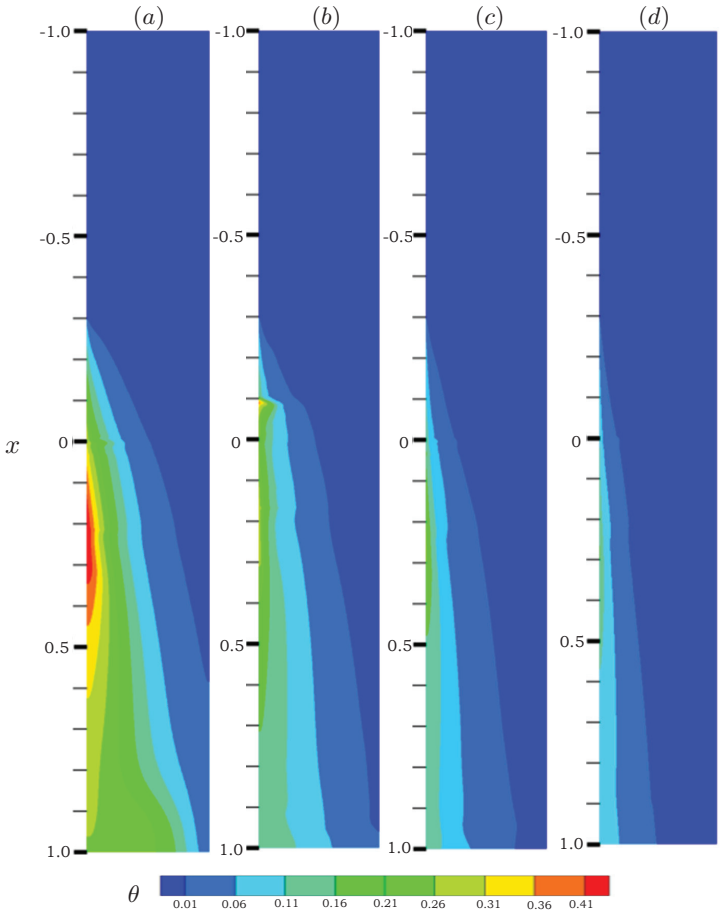

Fig. 9. Colored contours of the time-averaged dimensionless temperature in the central section at $z = 0$ m for $\mathrm{Gr} = 2.88 \cdot 10^7$, $\mathrm{Ha} = 660$: (*a*) $\mathrm{Re} = 3040$, (*b*) $\mathrm{Re} = 6080$, (*c*) $\mathrm{Re} = 9120$, (*d*) $\mathrm{Re} = 15200$.

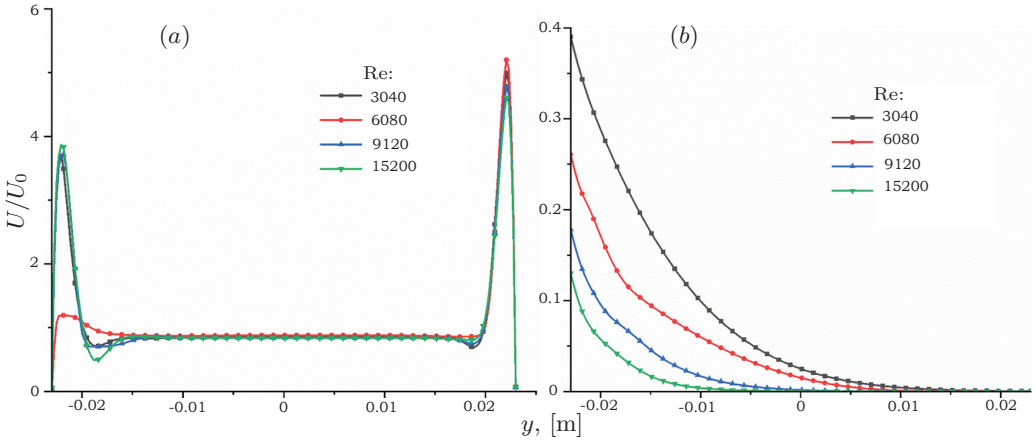

Fig. 10. Profiles of (*a*) time-averaged velocity and (*b*) time-averaged temperature along the y-axis at $x = 0.1$ m and $z = 0$ m for $\mathrm{Gr} = 2.88 \times 10^7$, $\mathrm{Ha} = 660$.

bulent vortex structure, with their axes aligning parallel to the direction of the magnetic field. As a result of buoyancy effects, these vortices concentrate on the side of the hot wall. The vortex structure extends along the streamwise direction at the fringing magnetic field zone near the inlet and outlet. There are more and more vortices near the hot wall in the heating zone ($-0.3\text{m} \le x \le 0.3\,\text{m}$) with Re increasing. The increase in vorticity reflects an increase of turbulence. As shown in Table 1, Nu increases with the increase of Re, indicating that the cooling effect of the liquid metal on the hot wall is enhanced.

3.3. Grashof number effects on mixed convection. Fig. 12 illustrates that the velocity profile in the duct has almost the same distribution. However, it is evident that this phenomenon changes near the outlet of the duct (at $x = 0.9\,\text{m}$) with a variation in Gr. As Gr rises, the fluid velocity on the left wall decreases. The forced convection is decreased by the buoyancy effect. As a result, it is possible to anticipate that the reverse flow would eventually appear close to the left side of the duct as Gr continues to rise.

Fig. 13 shows the dimensionless time-averaged temperature at the center section of the duct. With an increase in Gr, the maximum dimensionless temperature at the hot wall rises accordingly. This is because the intensified buoyancy effect supersedes the forced convection. Buoyancy effects decrease the cooling effect of liquid metal on the heating wall. With increasing Gr at the duct outlet section ($x > 0.8\,\text{m}$), the temperature distribution becomes more homogeneous. Moreover, a stronger heat transfer towards the right highlights the amplification of the transverse heat transfer along the y-axis due to the buoyancy effect.

Fig. 14*a* shows that the high-velocity jet near the heating wall gradually decreases with the increase of Gr. This indicates that the increase of buoyancy further suppresses the high-velocity jets in the side layers. On the other side, the velocity jet does not change obviously with Gr in the simulation parameter range. As seen in Fig. 14*b*, the temperature on the heating wall steadily rises, but there is no noticeable variation in the transmission range along the y-axis. The difference of the temperature profile is relatively small due to the slight difference in magnitude of Gr numbers.

3.4. Pressure drop coefficients and scaling law of the Nusselt numbers. Fig. 15 reveals that the pressure drop near the inlet and outlet is significantly lower in comparison to the uniform magnetic zone. Additionally, for the same Re and Gr, as seen in Cases 1–4, the pressure rises with an increase in Ha because the inhibitory impact on the fluid flow in the duct is amplified by the rise in the magnetic field intensity. The pressure increases with Re with the same Ha and Gr, as shown for Cases 3 and 5–7. Re increases, which is a result of the pump's power increase to move the flow of liquid metal faster. As evidenced by Cases 6, 8, and 9, there was no appreciable variation in pressure under different Gr at the same Ha and Re.

The MHD pressure drop coefficient is defined as

$$K = \frac{\Delta p / \Delta x}{\sigma U_0 B_0^2}. \tag{23}$$

The normalized pressure drop coefficient between $-0.6\text{m} \le x \le 0.6\,\text{m}$ is summarized in Table 2. It shows that the normalized pressure drop coefficient does not vary significantly in the simulation parameters range.

The average Nu number on the heating wall surfaces for all cases is listed in the last column in Table 1. The Nu number increases from 2.978 to 4.78 monotonically, as Ha increases from 220 in Case 1 to 1100 in Case 4. The velocity jet near the heating wall

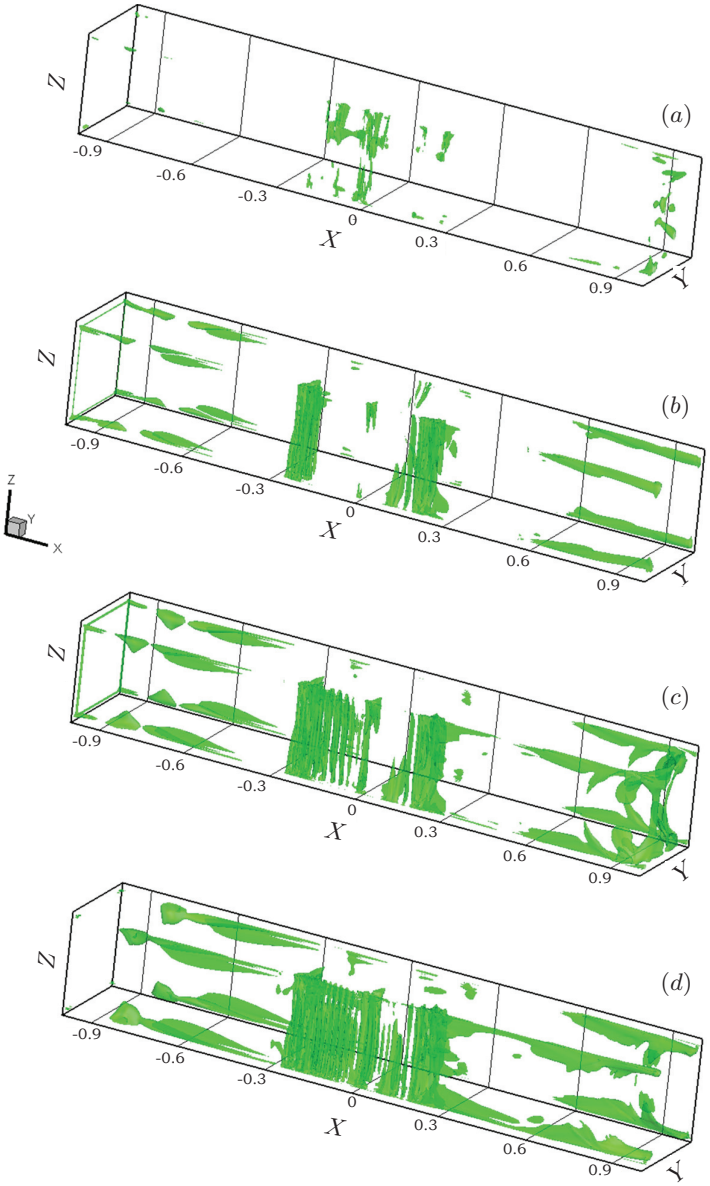

Fig. 11. Distribution of Liutex along the duct for R = 0.2 at Gr = $2.88 \cdot 10^7$, Ha = 660, $z = 0$ m. (*a*) Re = 3040, (*b*) Re = 6080, (*c*) Re = 9120, (*d*) Re = 15200.

Table 2. Normalized pressure drop coefficient.

	Case 1	Case 2	Case 3	Case 4	Case 5	Case 6	Case 7	Case 8	Case 9
K	0.119	0.096	0.089	0.087	0.091	0.088	0.091	0.091	0.092

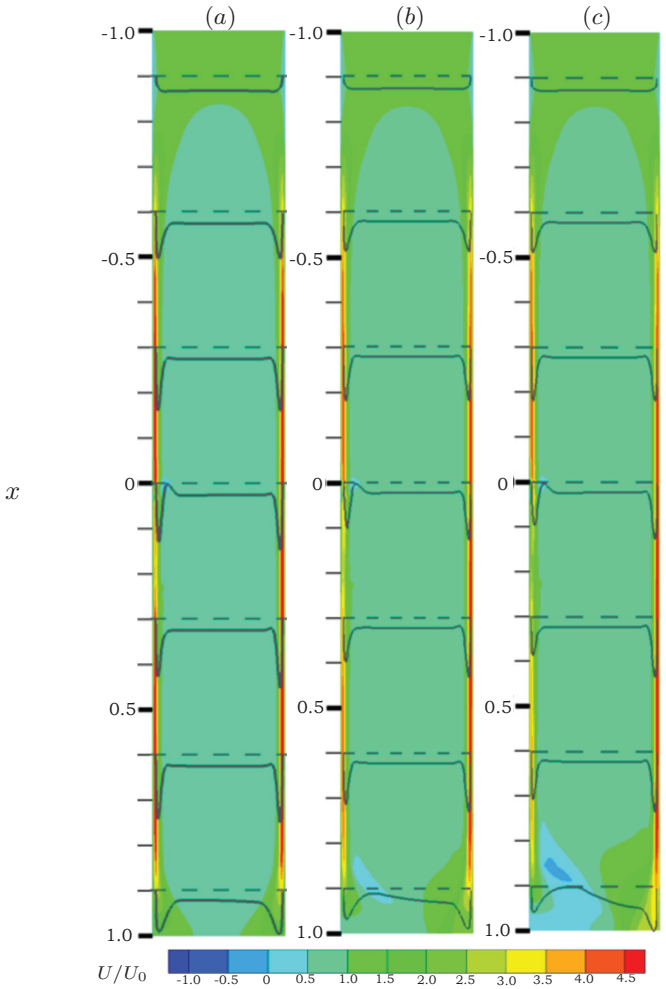

Fig. 12. Colored contours of the time-averaged dimensionless temperature in the central section at $z = 0$ m for Ha = 660, Re = 9120: (*a*) Gr = $2.88 \cdot 10^8$, (*b*) Gr = $1.44 \cdot 10^8$, (*c*) Gr = $2.88 \cdot 10^8$. The black dashed line is a reference line taken every 13 characteristic lengths. The black solid lines represent the velocity profile of the reference line (these velocity solid lines are uniformly scaled to ensure readership).

increases with Ha increase (Fig. 5), and the convective heat transfer along the streamwise direction enhances (Fig. 6). As a result, Nu increases.

As Re increases from 3040 in Case 3 to 15200 in Case 7 at Ha = 660 and Gr = $2.88 \cdot 10^7$, Nu also increases monotonically from 4.42 to 5.46, 7.09 and 8.8. As illustrated in Fig. 9, the forced convective heat transfer in the streamwise direction intensifies with the increase in Re. As a result, the Nu number increases as the Re number increases.

The Gr number increases from $2.88 \cdot 10^7$ in Case 6 to $1.44 \cdot 10^8$ and $2.88 \cdot 10^8$ in Case 8 and Case 9 at Ha = 660 and Re = 9120, Nu remains relatively constant within the range of simulations, and the differences between them are within 5%. The effect of Gr on convective heat transfer on the heating wall is insignificant in this range. However, Nu may show a downward trend as Gr increases because the enhanced buoyancy effect weakens forced convection.

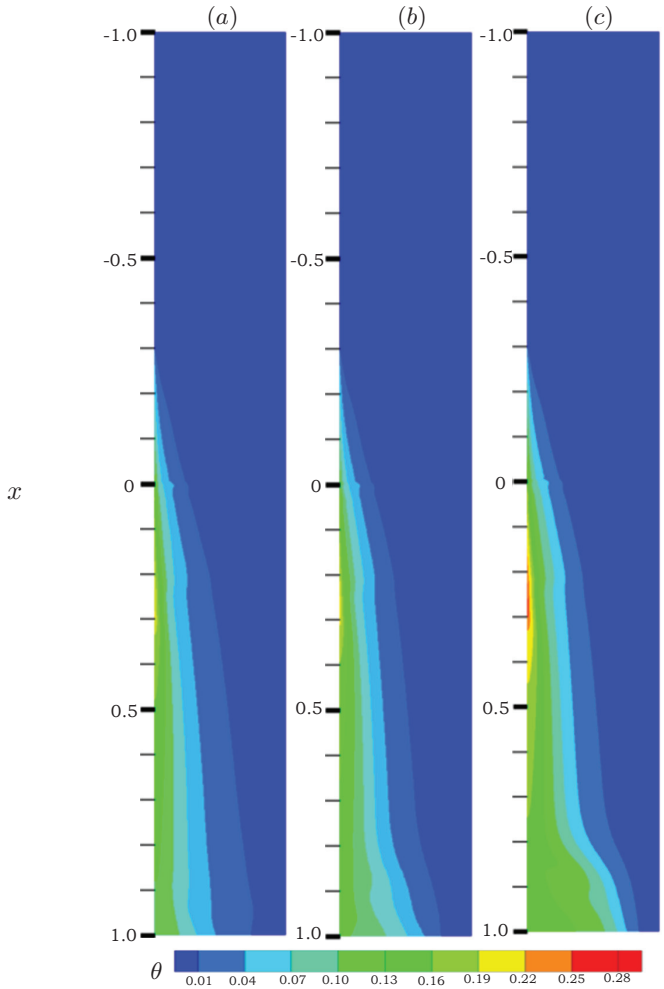

Fig. 13. Colored contours of the dimensionless time-averaged temperature in the central section at $z = 0$ m for Ha = 660, Re = 9120: (*a*) $\mathrm{Gr} = 2.88 \cdot 10^7$, (*b*) $\mathrm{Gr} = 1.44 \cdot 10^8$, (*c*) $\mathrm{Gr} = 2.88 \cdot 10^8$.

Sahu [26] presented a reverse power law of

$$\mathrm{Nu} = \left(\frac{\mathrm{Gr}}{\mathrm{Ha}^2 \mathrm{Re}^2} \right)^{-0.074}$$

according to the experimental results of the liquid metal MHD flow in a horizontal square duct. The Nu number values obtained in this paper, varying with , are presented in Fig. 16. Nu follows the law well at $\mathrm{Gr} = 2.88 \cdot 10^7$:

$$\mathrm{Nu} = 0.282 \left(\frac{\mathrm{Gr}}{\mathrm{Ha}^2 \mathrm{Re}^2} \right)^{-0.227} \tag{24}$$

The Nu number in Cases 8 and 9 does not fit the line because it varies insignificantly in the range of Gr.

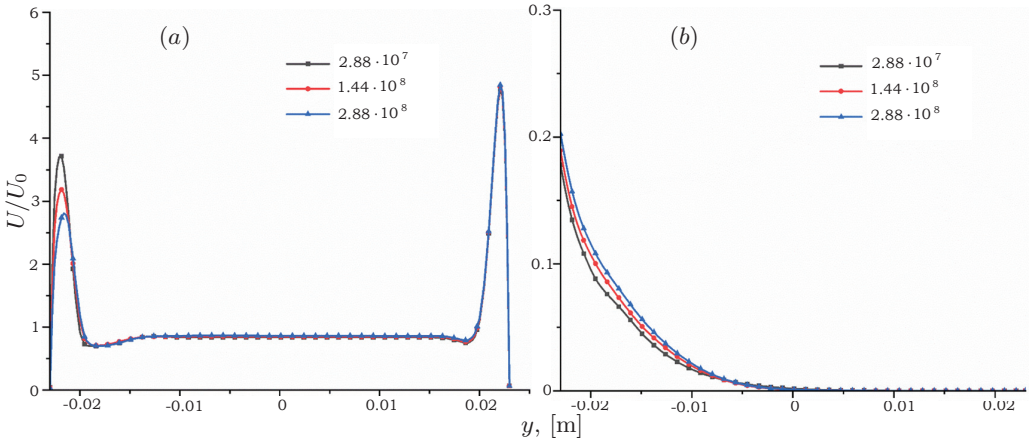

Fig. 14. Profiles of (a) time-averaged velocity and (b) time-averaged temperature along the y-axis at $x = 0.1$ m and $z = 0$ m for $\mathrm{Gr} = 2.88 \times 10^7$, $\mathrm{Ha} = 660$.

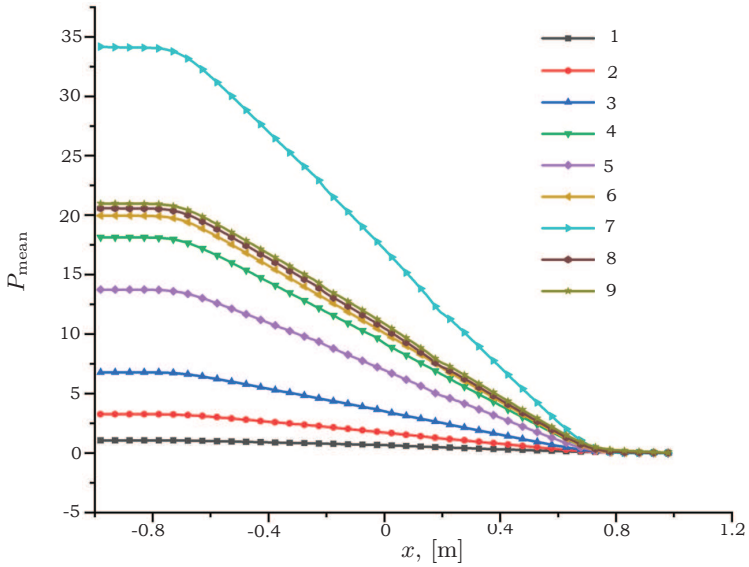

Fig. 15. Pressure distributions along the central axis at $y = 0$, $z = 0$.

4. Conclusions.

A SSTMHD turbulence model based on the SST k-ω model has been developed and implemented in OpenFOAM. A benchmark case was selected to verify and validate the model. With a non-uniform magnetic field and a constant heat flux, we simulated an MHD mixed convection flow in a square duct with electric conducting walls using the SSTMHD model. The temperature and velocity from the model and DNS results have been compared.

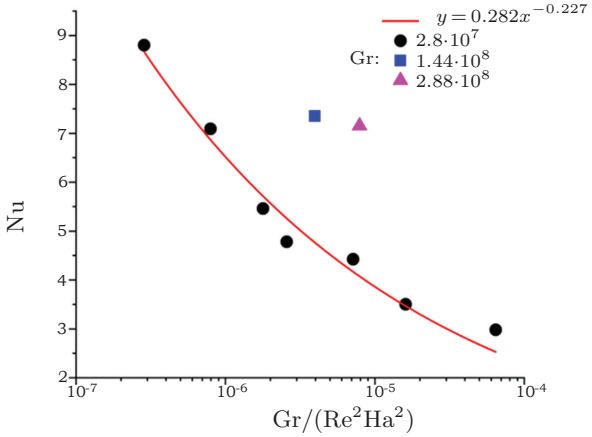

Fig. 16. Functional relationship of Nu with $\mathrm{Gr}/(\mathrm{Re}^2\mathrm{Ha}^2)$.

In general, the developed SSTMHD model can effectively simulate the temperature distribution and velocity variation of the magnetohydrodynamic turbulent flow coupling the fluid, solid, temperature field and electromagnetic field. The model can be used to simulate the MHD mixed convection flow subjected to a strong non-uniform magnetic field and strong heat source, such as a liquid metal blanket and a liquid metal MHD power generator.

Subsequently, the new model was utilized to investigate the impacts of Ha (220–1100), Re (3040–15200), and Gr (2.88×10^7–2.88×10^8) on the velocity distribution, temperature distribution, and heat transfer efficiency of the fluid in a vertical conducting duct under mixed convection.

The peak velocity of the jet and reverse flow in the duct increases with the increase of the Ha number, but they also slow down the development of reverse flow zones. The distance of horizontal heat transfer becomes closer as Ha increases. Overall, the Ha number stabilizes the flow. Although the Nu number of the wall increases as the Ha increases, the growth rate of Nu gradually decreases.

At high Re numbers, the flow adjacent to the heated wall remains in a robust turbulent state and undergoes a transition to forced convection. As the Re number increases, the Nu number near the hot wall increases, too. While the transverse heat transmission along the y-axis decreases, the heat transfer of the liquid metal along the flow direction strengthens. The heat transfer efficiency at the hot wall increases with the increase of Re.

When the Gr number is between 10^7 and 10^8, the flow field in the duct remains almost unchanged except the zone near the outlet. At the hot wall, the Gr number has a negligible impact on the Nu number.

A functional relationship exists between Nu numbers and these dimensionless parameters. Compared to the Gr number, Re has a more significant impact on Nu within the parameter range studied in this research. Moreover, it is necessary to simulate more cases with a much higher Gr number in the future.

Acknowledgments.

The authors acknowledge the support of the National Natural Science Foundation of China (NSFC) under Grant No. 11375049 and the National Magnetic Confinement Fusion Science Program of China under Grant No. 2014GB125003.

References

[1] M. Abdou, N.B. Morley, S. Smolentsev, A. Ying, S. Malang, A. Rowcliffe, M. Ulrickson. Blanket/first wall challenges and required R&D on the pathway to DEMO. *Fusion Engineering and Design*, vol. 100 (2015), pp. 2–43.

[2] N. Razuvanov, P. Frick, I. Belyaev, V. Sviridov. Experimental study of liquid metal heat transfer in a vertical duct affected by coplanar magnetic field: downward flow. *International Journal of Heat and Mass Transfer*, vol. 143 (2019), pp. 118529.

[3] L. Giancarli, M. Abdou, D. Campbell *et al.* Overview of the ITER TBM Program. *Fusion Engineering and Design*, vol. 87 (2012), pp. 395–402.

[4] O. Zikanov, I. Belyaev, Y. Listratov, P. Frick, N. Razuvanov, V. Sviridov. Mixed convection in pipe and duct flows with strong magnetic fields. *Applied Mechanics Reviews*, vol. 73 (2021), no. 1, p. 010801.

[5] X. Zhang, O. Zikanov. Convection instability in a downward flow in a vertical duct with strong transverse magnetic field. *Physics of Fluids*, vol. 30 (2018), p. 117101.

[6] N. Singh, M.K. Khandelwal, A.K. Sharma. Magnetohydrodynamic mixed convection flow of liquid metals in a vertical channel: a stability analysis. *International Journal of Mechanical Sciences*, vol. 234 (2022), pp. 107657.

[7] W. Guo, H.-M. Prasser. Direct numerical simulation of turbulent heat transfer in liquid metals in buoyancy-affected vertical channel. *International Journal of Heat and Mass Transfer*, vol. 194 (2022), pp. 123013.

[8] S. Kenjereš. On modeling and eddy-resolving simulations of flow, turbulence, mixing and heat transfer of electrically conducting and magnetizing fluids: a review. *Int. J. Heat and Fluid Flow*, vol. 73 (2018), pp. 270–297.

[9] H.-C. Ji, R. Gardner. Numerical analysis of turbulent pipe flow in a transverse magnetic field. *International Journal of Heat and Mass Transfer*, vol. 40 (1997), pp. 1839–1851.

[10] S. Kenjereš, K. Hanjali. On the implementation of effects of Lorentz force in turbulence closure models. *Int. J. Heat and Fluid Flow*, vol. 21 (2000), pp. 329–337.

[11] Z. Meng, S. Zhang, J. Jia, Z. Chen, M. Ni. AK-Epsilon RANS turbulence model for incompressible MHD flow at high Hartmann number in fusion liquid metal blankets. *International Journal of Energy Research*, vol. 42 (2018), pp. 314–320.

[12] Z. Chen, J. Zhang, C. Lee. Direct numerical simulation of the turbulent MHD channel flow at low magnetic Reynolds number for electric correlation characteristics. *Science China Physics, Mechanics and Astronomy*, vol. 53 (2010), pp. 1901–1913.

[13] Z. Chen. Nonlinear eddy viscosity$k$-ωturbulence model for incompressible low ReM magnetohydrodynamic flows. *Scientia Sinica Physica, Mechanica and Astronomica*, vol. 41 (2011), pp. 995.

[14] X.W. Zhang, J. Mao, L. Yu. A new k-ω model for magnetohydrodynamic turbulent duct flow. In: *Applied Mechanics and Materials, Trans. Tech. Publ.*, (2017), pp. 253–256.

[15] J. Mao, S. Aleksandrova, S. Molokov. Joule heating in magnetohydrodynamic flows in channels with thin conducting walls. *International Journal of Heat and Mass Transfer*, vol. 51 (2008), pp. 4392–4399.

[16] W.K. Hussam, G.J. Sheard. Heat transfer in a high Hartmann number MHD duct flow with a circular cylinder placed near the heated side-wall. *International Journal of Heat and Mass Transfer*, vol. 67 (2013), pp. 944–954.

[17] T.J. Rhodes, G. Pulugundla, S. Smolentsev, M. Abdou. 3D modelling of MHD mixed convection flow in a vertical duct with transverse magnetic field and volumetric or surface heating. *Fusion Engineering and Design*, vol. 160 (2020), p. 111834.

[18] S. Smolentsev, T. Rhodes, Y. Yan *et al.* Code-to-code comparison for a PbLi mixed-convection MHD flow. *Fusion Science and Technology*, vol. 76 (2020), pp. 653–669.

[19] M. Jischa, H.B. Rieke. About the prediction of turbulent Prandtl and Schmidt numbers from modeled transport equations. *International Journal of Heat and Mass Transfer*, vol. 22 (1979), pp. 1547–1555.

[20] M.-J. Ni, R. Munipalli, N.B. Morley, P. Huang, M.A. Abdou. A current density conservative scheme for incompressible MHD flows at a low magnetic Reynolds number. Part I: On a rectangular collocated grid system. *Journal of Computational Physics*, vol. 227 (2007), pp. 174–204.

[21] J. Mao, Y. Cheng, L. Xie. Natural convection of MHD flow in a long vertical closed duct with different wall conductance ratios. *Magnetohydrodynamics*, vol. 57 (2021), 3, pp. 449–466.

[22] M.-J. Ni, R. Munipalli, P. Huang, N.B. Morley, M.A. Abdou. *A current density conservative scheme for incompressible MHD flows at a low magnetic Reynolds number. Part II: On an arbitrary collocated mesh. Journal of Computational Physics*, vol. 227 (2007), pp. 205–228.

[23] T.J. Rhodes, G. Pulugundla, S. Smolentsev, M. Abdou. 3D modelling of MHD mixed convection flow in a vertical duct with transverse magnetic field and volumetric or surface heating. *Fusion Engineering and Design*, vol. 160 (2020), p. 111834.

[24] C. Liu, Y. Gao, S. Tian, X. Dong. Rortex – a new vortex vector definition and vorticity tensor and vector decompositions. *Physics of Fluids*, vol. 30 (2018), p. 035103.

[25] C. Liu, Y.-S. Gao, X.-R. Dong *et al.* Third generation of vortex identification methods: Omega and Liutex/Rortex based systems. *Journal of Hydrodynamics*, vol. 31 (2019), pp. 205–223.

[26] S. Sahu, C. Courtessole, A. Ranjan *et al.* Thermal convection studies in liquid metal flow inside a horizontal duct under the influence of transverse magnetic field. *Phys. Fluids*, vol. 32 (2020), p. 067107.

Received 25.10.2023